Flexible and Printed Electronics

PAPER

A printed wireless fluidic pressure sensor

Flexible and Printed Electronics

PAPER

A printed wireless fluidic pressure sensor

Yichen Zhai, Jiyeon Lee, Quyen Hoang, Dan Sievenpipper, Harinath Garudadri and Tse Nga Ng

Department of Electrical and Computer Engineering, Jacobs Hall, 9500 Gilman Drive, University of California San Diego, La Jolla, CA 92093, United States of America

E-mail: tnn046@ucsd.edu

RECEIVED
2 July 2018

REVISED
6 September 2018

ACCEPTED FOR PUBLICATION
12 September 2018

PUBLISHED
27 September 2018

Keywords: LC resonator, porous dielectric, wireless pressure sensor

Supplementary material for this article is available online

Abstract

An inkjet-printed inductor–capacitor (LC) resonator is demonstrated for wireless monitoring of pressure in aqueous environments. The sensing mechanism is based on a compressible capacitor that modulates the LC circuit resonant frequency depending on the applied pressure. The trace conductivity and geometric designs of inductors are improved to increase mutual inductive coupling between the sensor and the readout coil. The dielectric porosity in the capacitive sensors are tuned to enhance pressure sensitivity. The encapsulated sensor showed a linear response to pressure between 30 and 170 mmHg (4–23 kPa) with respect to atmospheric pressure and a resolution of 3 mmHg. The sensor temporal response is up to 6 Hz and capable of capturing typical heart-pulse waveforms as a proof-of-concept demonstration.

Wireless monitoring of physiological pressure is highly desirable for preventing failure of implanted prosthetic grafts. For example, prosthetic vascular shunts are prone to clogging in patients undergoing renal hemodialysis, but monitoring procedures using ultrasound or x-ray angiograms are costly and not suitable for frequent use to enable early detection of failing grafts [1]. Wireless telemetry based on inductor–capacitor (LC) resonators [2–6] provides convenient monitoring of the grafts, in which sensor signals are measured through inductive coupling with an external reader. Passive LC resonator circuits are limited in transmission distances but can be used for subcutaneous grafts [1, 7] that are typically less than 2 cm from the skin surface. The LC resonators occupy a smaller footprint and are simpler to fabricate than active devices for integration with mechanically flexible, space-constrained grafts.

In this work we demonstrate a printed LC resonator to measure hemodynamic pressure. The pressure sensing component is a compressible capacitor, such that the capacitance increases under pressure and in turn modulates the resonance frequency of the LC resonator. There are other pressure sensing devices based on resistive [8–12] or piezoelectric mechanisms, [13] but wireless detection of the corresponding resistance change, such as in liquid–metal sensors, [11, 12] or induced voltage requires a more complex circuit than the LC resonator. Prior research on polymeric capacitive pressure sensors [14–19] used micro-structures in dielectric materials to improve sensitivity. By using templates, the dielectric structural geometry is tuned to change its elastic moduli for various pressure sensing applications. However, the sensors were porous and not designed to work in liquid conditions. Here we incorporate encapsulation and develop an fabrication process with inkjet printing, which reduces processing steps compared to conventional micro-electromechanical systems fabrication and allows rapid, reliable prototyping on flexible substrates. We designed a method of integration that combine the planar inductor pattern and porous foam capacitor in a geometric design that avoid vias and simplifies fabrication. We demonstrate printing toolpaths and an empirical model used to optimize the wireless coupling between the sensor and the readout inductor coils for maximal reading distance.

As shown in figure 1, the LC resonator consists of an inductor and two capacitors with microstructured dielectrics designed to enhance the pressure-induced change in capacitance. The two capacitors are connected in series through a common electrode. This configuration eliminates the need for an interconnect via between the top capacitor electrode layer to the

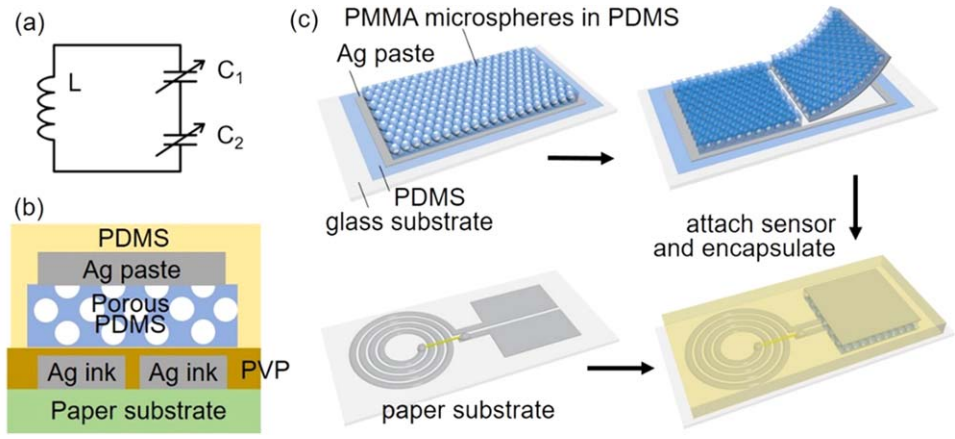

Figure 1. (a) Schematics of the LC resonator. (b) Cross-sectional view of the capacitive pressure sensing structure. (c) Schematics of the fabrication process.

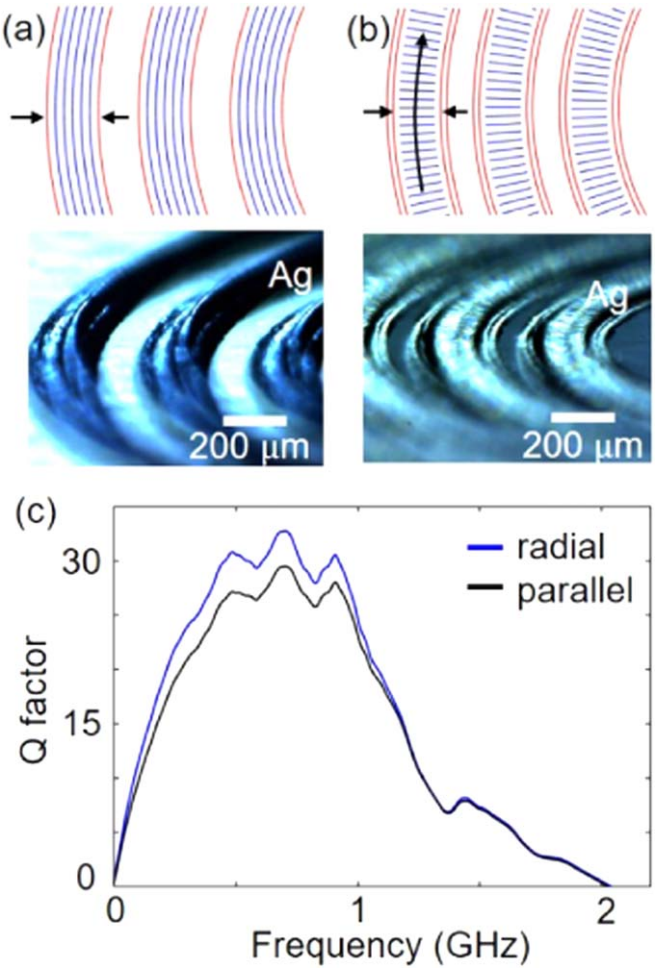

Figure 2. Printer toolpath in (a) parallel or (b) radial sequence, and photographs of the corresponding printed silver features. (c) Comparison of inductor quality factors when printing is done with radial or parallel toolpath.

inductor layer, thus simplifying fabrication compared to a single capacitor design. The key processing parameters that improve inductor and capacitor characteristics are discussed below, while details of the fabrication procedure are provided in the experimental section.

The inductor is patterned by printing silver ink on a flexible paper substrate, and the printhead toolpath affects ink reflow and the resulting conductor trace profile [20–22]. Based on the geometric inductance expressions from [23], we make the inductor a four-turn Archimedian spiral with an outer diameter of

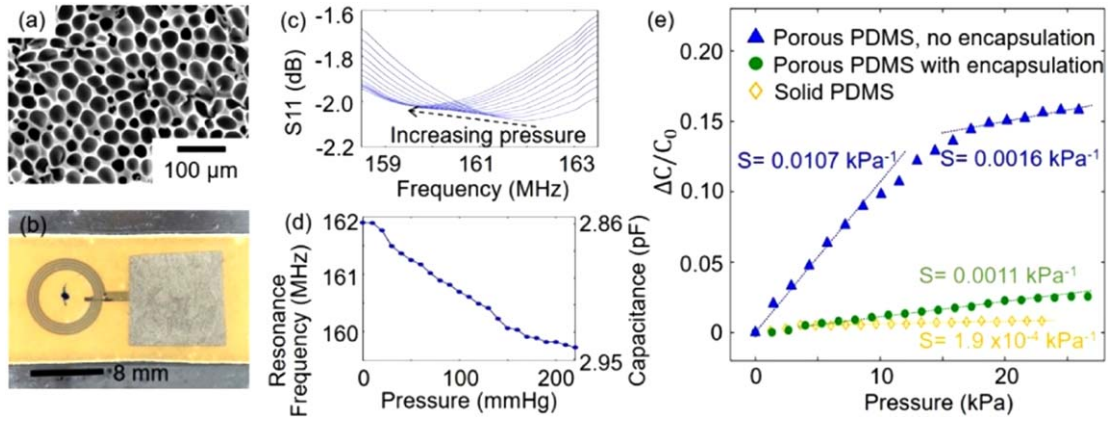

Figure 3. Scanning electron micrograph of the porous PDMS dielectric. (b) Photograph of the encapsulated LC resonator. (c) Reflection coefficient versus resonance frequency at a reading distance of 3 mm between the readout coil and encapsulated LC resonator. The applied pressure on the sensor is increased from 0 mmHg, in increments of 20 mmHg, with respect to atmospheric pressure. (d) Resonance frequency and capacitance versus applied pressure, extracted from part (c). (e) Relative capacitance versus pressure for sensors with different dielectrics or encapsulation.

8.1 mm, trace width of 210 μm, and thickness of 10 μm, expecting an inductance of 196 nH in frequency range below 10 MHz. When inkjet printing on the paper surface, each Ag droplet forms a dot with diameter about 50 μm and thickness around 1.5 μm. Thus multiple printing passes are required to fill out the spiral pattern and build up the trace thickness. The printer toolpath starts with defining the edges of each trace. Then two different sequences of ink deposition are characterized in figure 2. For the parallel toolpath, when a new line is being printed, the ink droplets land on the side of a previous line that has already dried, leading to a stacked morphology. In contrast, for the radial toolpath, the line segments are short and new ink is added before the previous line dries, allowing ink reflow that results in a smooth surface. Figure 2(c) shows the measured inductor quality factor $Q = \omega L/R$, where ω is the angular frequency and R is the trace resistance at a specific frequency. The Q of the inductor made with radial sequence is better than the one with parallel sequence, because the radial toolpath enables a smooth conductor surface that reduces electron scattering and trace resistance.

The pressure sensing capacitors are made with a porous elastomer for measurement between 30 and 170 mmHg, or 4 and 23 kPa, with respect to atmospheric pressure; this range spans the blood pressure values for children and adults. The elastomer polydimethylsiloxane (PDMS) solution is mixed with sacrificial polymethyl mathacrylate (PMMA) microspheres. After annealing, the film is submerged in dichlorobenzene, which does not damage the crosslinked PDMS but dissolve away the PMMA microspheres to leave behind pores in the dielectric (figure 3). The estimated air-void volume is 55% of the film, based on the solid content ratio of PDMS to PMMA. This approach [16, 18] to form micro-pores increases the capacitance change compared to a solid dielectric, because the elastic modulus is decreased in porous films. The integrated LC resonator is encapsulated with PDMS to seal the edges of the capacitor and prevent environmental liquids from flowing into the porous dielectric.

By inductive coupling, power is transmitted wirelessly from a readout coil to the sensor coil and induces resonance in the sensor circuit. The sensor resonant frequency f_s is related to the sensor's inductance L and capacitance C by [3]

$$f_s = \frac{1}{2\pi\sqrt{LC}}. \quad (1)$$

The readout system records the power reflection over the input frequency spectrum. At the readout coil terminals, the input reflection coefficient S11 is lowest near the sensor resonant frequency where the sensor absorbs the most power from the readout coil. The frequency at the S11 minimum depends on sensor L, C by [24]

$$f_{\mathrm{S11\,min}} = (1 + 1/8Q^2 + k^2/4)f_s, \quad (2)$$

where k is the geometry-dependent coupling coefficient between 0 (no coupling) and 1 (maximum coupling) [3, 4]. Since $1/8Q^2 + k^2/4 \ll 1$ in normal circumstances, we can justify equating f_{S11min} to f_s. Upon applying pressure to the sensor inside a water chamber, the resonant frequency shifts to lower values (figure 3(c)). The corresponding capacitance versus applied pressure is calculated from equation (1) with a measured $L = 337$ nH at 162 MHz, as shown in figure 3(d). The initial capacitance C_0 is 2.86 pF for our pressure sensor with a total area of 8×8 mm^2. The calculated capacitance is the total capacitance of the LC circuit loop, including parasitic capacitance between inductor turns and contributions from adhesion layers that are not sensitive to pressure. Hence the capacitance sensitivity to pressure is lower in the integrated wireless LC resonator than in discrete capacitive sensors.

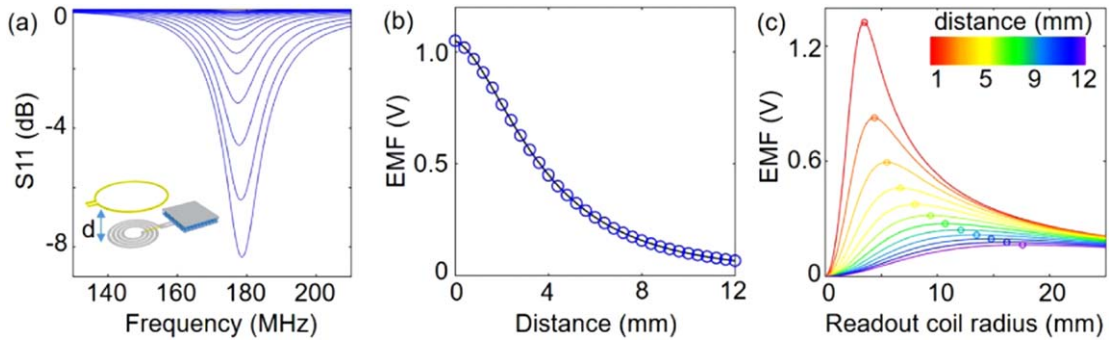

Figure 4. (a) Reflection coefficient versus frequency, as the distance *d* between the sensor and the readout coil is varied from being in contact to 12 mm apart, in steps of 1 mm. The inset shows the measurement setup. (b) Electromotive potential induced on the sensor versus reading distance, for a readout coil with radius of 5.3 mm. The line is a fit to the electromotive force (EMF) function derived in the supplementary material. (c) Electromotive potential EMF(d, r_r) induced on the sensor coil with a radius of 4 mm versus readout coil radius r_r. The set of curves shows the results as reading distance is increased from 1 mm (red) to 12 mm (blue).

The sensitivity of a capacitive sensor is defined as $S = \delta(\Delta C/C_0)/\delta P$, where $\Delta C = C(P) - C_0$ is the capacitance change at an applied pressure P, with respect to the initial capacitance. The sensitivity values are denoted in figure 3(e). To demonstrate the elastic property of the PDMS porous foam, we measured the sensor response under 40 mmHg mechanical pressure over 12 cycles, and the repeatable response is shown in supplementary figure S2, available online at stacks.iop.org/FPE/3/035006/mmedia. Previous works have also shown that PDMS foam capacitors have high repeatability without hysteresis over 1000–15 000 cycles [14, 16, 17]. The sensors with porous PDMS show better sensitivity by at least an order of magnitude than the one with un-structured dielectric. The LC resonator needs an encapsulation for stable operation in liquids, but the encapsulation significantly reduces the sensitivity at low pressure range <15 kPa (or <112 mmHg). Without encapsulation, the air inside the dielectric can readily escape as pressure is applied, while in the encapsulated device the volume is less compressible due to trapped air. Previous work [25] has improved sensitivity by using additional air reservoirs at the expense of sensor dimensions.

For high pressure range >15 kPa or >112 mmHg, the unencapsulated sensor saturates as the air voids are diminished, reducing the elasticity of the dielectric and in turn lowering sensitivity. The sensitivity of the capacitive pressure sensors here is low compared to other non-sealed sensors, because air gap between dielectric and electrode in prior work [14–18] can increase sensitivity. The response of the un-structured device matches well with the mechanical modulus as measured in [26]. Several aspects, such as sealing under partial vacuum and reducing thicknesses of the top electrode and encapsulation layers to increase electrode displacement, can potentially improve performance in the future. Nonetheless, at the current sensitivity level of 0.011 MHz mmHg^{-1} and a background noise of 0.03 MHz, the integrated LC resonators are capable of resolving 3 mmHg, sufficient for blood pressure monitoring in prosthetic graft applications.

To determine the wireless readout range, the S11 response is measured as the reading distance d between the sensor and the readout coil is raised (figure 4). At a very close distance where the coupled power transfer between the readout and sensor coil is high, the S11 shows sharp resonance response, with the readout coil impedance at 1.608 + j25.888 Ω at 177 MHz as measured in air. The inductive coupling is decreased with increasing reading distance, and the readout coil S11 is −0.162 dB at d = 12 mm and reaches the reading distance limit. The real part of readout coil input impedance at resonance frequency is $Re(Z_{in}) = 2\pi f_s L_r k^2 Q$, where L_r is the readout coil inductance. The coupling factor k is distance dependent and approximated [4] by $k = r_s^2 r_r^2/((d^2 + r_r^2)^{3/2}\sqrt{r_s r_r})$ for the case $r_s < r_r$, where r_s is the sensor coil radius and r_r is the readout coil radius. This expression indicates how longer reading distance changes the input impedance Z_{in} and in turn the magnitude of S11. The readout coil resonant frequency f_{S11min} is not significantly affected by reading distance, for k is typically small <0.35 and thereby $f_{S11min} \sim f_s$ (equation (2)).

The S11 magnitude at resonant frequency is converted to an induced electromotive force using $\text{EMF} = \sqrt{P_{dissipate} \times R} = \sqrt{P_{total}(1 - 10^{S_{11}/10})R}$, where P_{total} = 10 mW is the root mean square output power of the vector network analyzer into the readout coil and R = 129.1 Ω at d = 0 mm and R = 120.5 Ω for d > 4.4 mm. In the supplementary material a mathematical expression is derived from magnetic flux relations to describe EMF(r_r, d) as a function of the reading distance and the readout coil radius. The derived function fits well to the EMF data over the range of reading distances in figure 4(b). Using a sensor coil radius of 4 mm, the EMF(r_r, d) function is plotted in figure 4(c) to show the inter-related effect of readout coil radius and reading distance. As the readout coil radius increases, the induced EMF on the sensor reaches maximum at a longer reading distance.

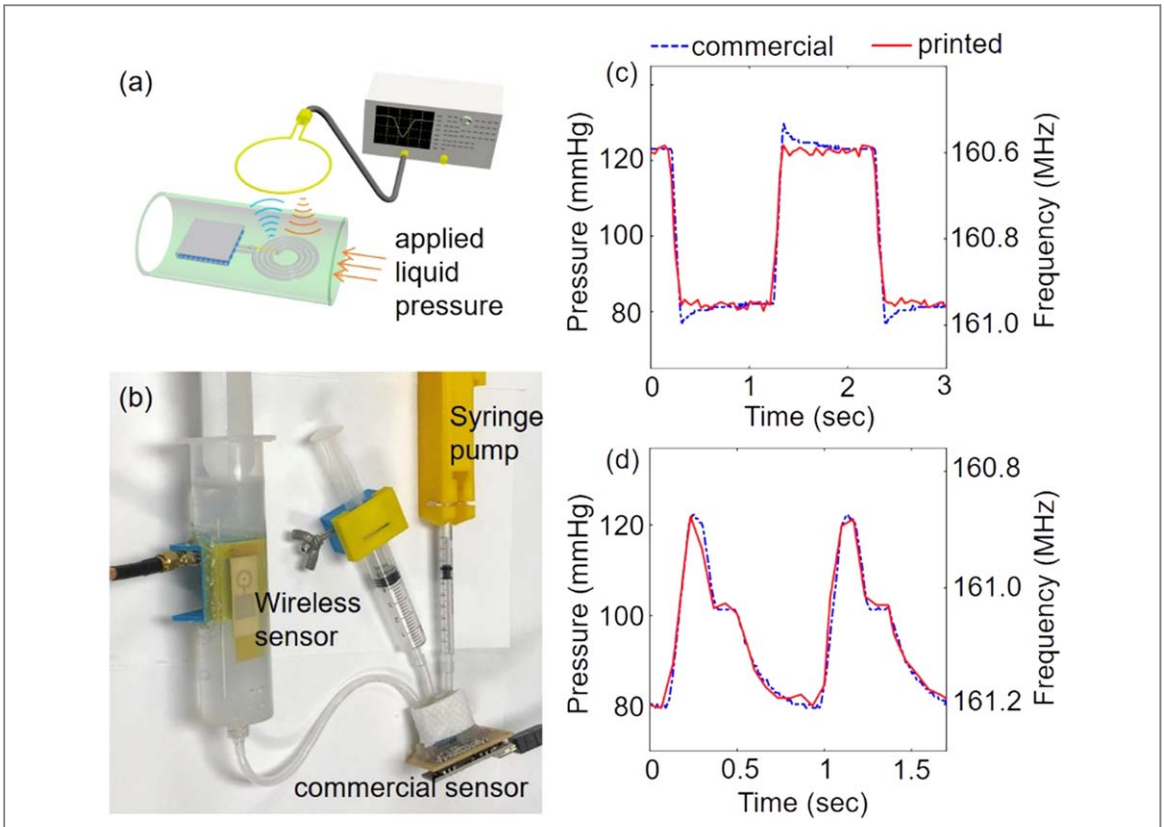

Figure 5. (a) Schematic and (b) photograph of the dynamic pressure measurement where the encapsulated LC resonator is inside a water-filled compartment. Temporal response of the sensors when (c) changing pressure in abrupt steps and (d) applying a presure profile that emulates heart pulses.

This function indicates that if we intend the reading distance to be farther, the radius of the readout coil should be wider; on the other hand, at close reading distances, a smaller readout coil radius is better for inducing higher EMF and stronger signals.

Moreover, the environment around the sensor can affect its capacitance and resonance frequency. For example, in figure 4(a), the distance response measurement was taken in air without a load, and the resonance frequency was about 178 MHz. In figure 3(c), the pressure measurement was taken with the same sensor in water. The resonance frequency lowered to 162 MHz without a load. As the sensor environment changed from air to water, the capacitance increased in the space around the sensor, because water has a higher dielectric constant than air. Thus, the frequency range can be shifted due to the sensor environment. Nonetheless, within aqueous environments, the encapsulated sensor shows consistent signals in response to pressure changes.

Dynamic pressure measurements is taken to characterize the response time of the encapsulated LC resonator inside a water-filled compartment (figure 5). Pressure pulses are applied by motor-driven plunger, to cycle the applied pressure between 80 and 120 mmHg. This range is typical for blood pressure in healthy adults. Our printed sensor closely tracks the pressure as reported by a commercial barometer. Under a step change in pressure (figure 5(c)), the rise and fall time of our LC resonator is 0.133 ± 0.033 s, and thus the sensor is capable to sample up to 6 Hz, which is more than enough for physiological monitoring since the maximum heart rate should be below 200 beats per minute or 3.3 Hz. A pressure profile that is similar to a heartbeat with systolic and diastolic blood pressure changes is applied and accurately recorded by the printed sensor in figure 5(d). The next step for this wireless telemetry development is to characterize the printed sensor response in lossy environment such as inside biological tissues. Moreover, with the small form factor and scalability, multiple sensors working operating at different resonant frequencies can be used together to detect pressure changes or flow along a fluidic path.

In summary, this work achieved an inkjet-printed wireless pressure sensor working in a water environment. We improved printing toolpaths and tuned the dielectric porosity in the capacitive sensor to realize a LC resonator that can resolve 3 mmHg with respect to atmospheric pressure. We also derived the optimal readout coil radius in relation to mutual inductive coupling at a certain reading distance. The sensor showed a linear response to pressure between 30 and 170 mmHg, with a sensitivity of 0.011 MHz $mmHg^{-1}$. The sensor temporal response is up to 6 Hz and capable of capturing the details of typical heart-pulse pressure profile as a proof-of-concept demonstration.

Experimental section

Fabrication of LC sensor

Nanoparticle silver ink (Novacentrix Metalon JS-B40G) was printed using piezoelectric inkjet [20, 21, 27, 28] (Fujifilm Dimatix DMP2800) on a paper substrate (Epson glossy photo paper) to pattern the four-turn inductor coil and the capacitor electrodes. After the ink was dried, polyvinylphenol (PVP, Aldrich) was spincoated to form a ~3 μm film over the Ag pattern to prevent delamination. The PVP solution consisted of 0.5 g PVP and 0.1 g of methylated polymelamine cross-linker in 5.4 g of propylene glycol monomethyl ether acetate solvent. The sample was annealed on a hot plate at 180 °C for 25 min. Parts of the PVP layer were mechanically scraped away to open via holes, and a piece of gold wire was used as a crossover interconnect to bridge one lead of the inductor coil to a capacitor electrode. The wire was connected to the electrodes by filling the vias with Ag ink.

A stretchable electrode coated with porous polydimethylsiloxane (PDMS) dielectric was prepared on a glass substrate prior to being transferred and bonded with the electrodes on the paper substrate. To fabricate the stretchable electrode [29], PDMS (Sylgard 184) was diluted with hexane in 1:2 ratio by weight, and spincoated on glass substrate as a buffer layer. The PDMS buffer layer was cured at 120 °C for 10 min. PDMS was mixed with silver paste (Ercon E2414 Ag/AgCl ink) in 1:7 weight ratio, and the mixture was blade coated onto the buffer layer of PDMS. The sample was cured at 120 °C for 30 min to form a Ag electrode ~60 μm in thickness. For the porous dielectric layer, polymethyl methacrylate (PMMA) microspheres with a diameter distribution of 27–32 μm (Cospheric PMPMS-1.2) was mixed with PDMS and hexane in 3:2:2 ratio by weight. The suspension was spincoated on the Ag electrode and heated at 100 °C for 1 h to obtain a dielectric film ~75 μm in thickness. After the PDMS was fully cross-linked by the thermal curing, the sample was placed in dichlorobenzene for 48 h to dissolve the PMMA microspheres, which left behind voids and hence the PDMS became a porous dielectric.

A piece of the Ag electrode with PDMS porous dielectric was cut, in order to be bonded to the paper substrate with the complementary capacitor electrodes and the inductor coil. The bonding process used a diluted PDMS solution (1:2 PDMS:hexane by weight) as the glue, which was spincoated at 2500 rpm for 2 min over the paper substrate. Subsequently the porous film was attached to the paper substrate and cured at 100 °C for 1 h under the weight from a piece of glass slide to facilitate even contact and securely bond the two parts together. Finally, a PDMS solution (2:1 PDMS:hexane by weight) was spincoated at 800 rpm for 2 min to encapulate the LC resonator. The structure was annealed at 100 °C for 1 h to complete the encapsulation process.

Characterization procedure

The impedance of individual inductors and capacitors was measured using a microwave probe (GGB Industries model 40A-GSG-250-DP) connected to a vector network analyzer (Agilent 8753ES). The S11 input reflection coefficient was measured using a one-turn readout coil with a diamater of 10.6 mm, with a resonance frequency of 162 MHz when sample was in water. The inductance of the readout coil is 337 nH at 162 MHz. The root mean square output power of the vector network analyzer was nominally 10 mW into the readout coil. The readout coil is placed parallel to the inductor of the LC resonator, with the coil centers aligned to each other during measurement.

Pressure pulses are applied using a home-built motor-controlled system, where three syringes were connected together (figure 5). The LC resonator was placed inside a water-filled syringe, and the compartment pressure was continuously monitored by a commercial barometer (Infineon Technologies Analog Absolute Pressure Sensor KP236N6165). The other syringes were filled with air to adjust pressure. The second syringe's plunger compressed air in the system, and upon reaching a baseline pressure the plunger was locked in position. The third syringe was used as a pump such that the plunger was driven by a stepper motor to apply pressure pulses. The motor and the commercial barometer were controlled and read by a microcontroller (Arduino Nano). The LC resonator was read wirelessly by the same one-turned readout coil described above, with the reading distance fixed at 3 mm. The vector network analyzer sampled at 16 Hz or 24 Hz. After sweeping frequency to track the resonant frequency f_{S11min}, the network analyzer was set to measure the S11 magnitude at 1 MHz higher than the resonant frequency. At a fixed frequency, we assumed that relative changes in S11 magnitude were correlated to a lateral shift of the S11 characteristics and extrapolated the S11 values to resonant frequency and capacitance by equation (1). Other telemetry methods [3] that directly measure resonant frequency are available, but here we chose the relative measurement due to the limited sampling rate in our off-the-shelf analyzer.

Acknowledgments

The authors are grateful for the support of the National Science Foundation under Division of Civil, Mechanical and Manufacturing Innovation grant #1635729.

ORCID iDs

Tse Nga Ng https://orcid.org/0000-0001-6967-559X

References

[1] Cheong J H *et al* 2012 An inductively powered implantable blood flow sensor microsystem for vascular grafts *IEEE Trans. Biomed. Eng.* **59** 2466–75

[2] Chen L Y, Tee B C K, Chortos A L, Schwartz G, Tse V, Lipomi D J, Wong H S P, McConnell M V and Bao Z 2014 Continuous wireless pressure monitoring and mapping with ultra-small passive sensors for health monitoring and critical care *Nat. Commun.* **5** 5208

[3] Huang Q-A, Dong L and Wang L-F 2016 LC passive wireless sensors toward a wireless sensing platform: status, prospects, and challenges *J. Microelectromech. Syst.* **25** 822–41

[4] Oliveira C C, Sepúlveda A T, Almeida N, Wardle B L, Da Silva J M and Rocha L A 2015 Implantable flexible pressure measurement system based on inductive coupling *IEEE Trans. Biomed. Eng.* **62** 680–7

[5] Tan Q, Luo T, Wei T, Liu J, Lin L and Xiong J 2017 A wireless passive pressure and temperature sensor via a dual LC resonant circuit in harsh environments *J. Microelectromech. Syst.* **26** 351–6

[6] Kim J, Wang Z and Kim W S 2014 Stretchable RFID for wireless strain sensing with silver nano ink *IEEE. Sens. J.* **14** 4395–401

[7] Khan M W A, Björninen T, Sydänheimo L and Ukkonen L 2016 Remotely powered piezoresistive pressure sensor: toward wireless monitoring of intracranial pressure *IEEE Microw. Wirel. Compon. Lett.* **26** 549–51

[8] Shintake J, Piskarev E, Jeong S H and Floreano D 2018 Ultrastretchable strain sensors using carbon black-filled elastomer composites and comparison of capacitive versus resistive sensors *Adv. Mater. Technol.* **3** 1700284

[9] Lee S *et al* 2016 A transparent bending-insensitive pressure sensor *Nat. Nanotechnol.* **11** 472–8

[10] Luo N, Zhang J, Ding X, Zhou Z, Zhang Q, Zhang Y-T, Chen S-C, Hu J-L and Zhao N 2018 Textile-enabled highly reproducible flexible pressure sensors for cardiovascular monitoring *Adv. Mater. Technol.* **3** 1700222

[11] Jung T and Yang S 2015 Highly stable liquid metal-based pressure sensor integrated with a microfluidic channel *Sensors* **15** 11823–35

[12] Zhou X P, Deng R S and Zhu J Y 2018 Three-layer-stacked pressure sensor with a liquid metal-embedded elastomer *J. Micromech. Microeng.* **28** 085020

[13] Ramadan K S, Sameoto D and Evoy S 2014 A review of piezoelectric polymers as functional materials for electromechanical transducers *Smart Mater. Struct.* **23** 033001

[14] Mannsfeld S C B, Tee B C K, Stoltenberg R M, Chen C V H H, Barman S, Muir B V O, Sokolov A N, Reese C and Bao Z 2010 Highly sensitive flexible pressure sensors with microstructured rubber dielectric layers *Nat. Mater.* **9** 859–64

[15] Kim J, Ng T N and Kim W S 2012 Highly sensitive tactile sensors integrated with organic transistors *Appl. Phys. Lett.* **101** 103308

[16] Kang S, Lee J, Lee S, Kim S G, Kim J K, Algadi H, Al-Sayari S, Kim D E, Kim D E and Lee T 2016 Highly sensitive pressure sensor based on bioinspired porous structure for real-time tactile sensing *Adv. Electron. Mater.* **2** 1600356

[17] Joo Y, Yoon J, Ha J, Kim T, Lee S, Lee B, Pang C and Hong Y 2017 Highly sensitive and bendable capacitive pressure sensor and its application to 1 V operation pressure-sensitive transistor *Adv. Electron. Mater.* **3** 1600455

[18] Atalay O, Atalay A, Gafford J and Walsh C 2018 A highly sensitive capacitive-based soft pressure sensor based on a conductive fabric and a microporous dielectric layer *Adv. Mater. Technol.* **3** 1700237

[19] Chen S, Zhuo B and Guo X 2016 Large area one-step facile processing of microstructured elastomeric dielectric film for high sensitivity and durable sensing over wide pressure range *ACS Appl. Mater. Interfaces* **8** 20364–70

[20] Soltman D and Subramanian V 2008 Inkjet-printed line morphologies and temperature control of the coffee ring effect *Langmuir* **24** 2224–31

[21] Graddage N, Chu T Y, Ding H, Py C, Dadvand A and Tao Y 2016 Inkjet printed thin and uniform dielectrics for capacitors and organic thin film transistors enabled by the coffee ring effect *Org. Electron.* **29** 114–9

[22] Ready S, Endicott F, Whiting G, Ng T N, Chow E and Lu J-P 2013 3D printed electronics *NIP & Digital Fabrication Conf.* vol 4, pp 9–12

[23] Mohan S S, Hershenson M D M, Boyd S P and Lee T H 1999 Simple accurate expressions for planar spiral inductances *IEEE J. Solid-State Circuits* **34** 1419–20

[24] Xue N, Chang S and Lee J 2012 A SU-8-based microfabricated implantable inductively coupled passive rf wireless intraocular pressure sensor *J. Microelectromech. Syst.* **21** 1338–46

[25] Lee H Y and Choi B 2015 Theoretical and experimental investigation of the trapped air effect on air-sealed capacitive pressure sensor *Sensors Actuators* A **221** 104–14

[26] Johnston I D, McCluskey D K, Tan C K L and Tracey M C 2014 Mechanical characterization of bulk Sylgard 184 for microfluidics and microengineering *J. Micromech. Microeng.* **24** 035017

[27] Ng T N *et al* 2015 Printed dose-recording tag based on organic complementary circuits and ferroelectric nonvolatile memories *Sci. Rep.* **5** 13457

[28] Ng T N, Schwartz D E, Mei P, Kor S, Veres J, Bröms P and Karlsson C 2016 Pulsed voltage multiplier based on printed organic devices *Flex. Print. Electron.* **1** 015002

[29] Wang K, Parekh U, Pailla T, Garudadri H, Gilja V and Ng T N 2017 Stretchable dry electrodes with concentric ring geometry for enhancing spatial resolution in electrophysiology *Adv. Healthcare Mater.* **6** 1700552